Supplemental Information for

Circularly Polarised Luminescent Inks with Low Crosstalk and High Efficiency for 3D Information Encoding from Liquid Crystal Microcapsules

Shenghao Hua[†a], Xiaojuan Wu[†b], Haixiao Yang[c], Yu Liu[a], Yinjie Chen*[a], Yajun Zhang*[c], Haifeng Yu*[d] and Quan Li*[e]

[a]Beijing Engineering Research Centre of Printed Electronics
Beijing Institute of Graphic Communication, Beijing, China
E-mail: chenyinjie@bigc.edu.cn

[b]Technology Innovation and Management Department
Beijing BOE Optoelectronics Technology CO., LTD.

[c]College of Mechanical and Electrical Engineering
Beijing University of Chemical Technology, Beijing, China
E-mail: zhyj@mail.buct.edu.cn

[d] School of Materials Science and Engineering, and Key Laboratory of Polymer Chemistry and Physics of Ministry of Education, Peking University, Beijing, China.
E-mail: yuhaifeng@pku.edu.cn

[e] Institute of Advanced Materials & School of Chemistry and Chemical Engineering
Southeast University, Nanjing, China.
E-mail: quanli3273@gmail.com

Contents

Experimental Section/Methods

Materials

The nematic liquid crystal HNG-720600 (Nanjing Ningcui Optical Technology Co., Ltd., Nanjing, China; n_e=1.574, n_o=1.477, T_{NI}=100℃) and the left-handed chiral dopant S5011 (Jiangsu Hecheng Display Technology Co., Ltd., Nanjing, China; HTP = 104 μm^{-1}) were purchased commercially. The fluorescent dye Rhodamine 6G, dichloromethane, PVA 1788, and methyl methacrylate (MMA) were purchased from Shanghai Macklin Biochemical Co., Ltd. (Shanghai, China). Azobis(isoheptanenitrile) (ABVN) was obtained from Shanghai Aladdin Biochemical Technology Co., Ltd. (Shanghai, China). All chemicals were used as received without further purification.

Preparation of Rhodamine 6G (R6G)-doped Cholesteric Liquid Crystals

The nematic liquid crystal was initially blended with the left-handed chiral dopant S5011 to form the CLC matrix, using dichloromethane as a co-solvent to facilitate the mixing process. To obtain CLCs exhibiting Bragg reflections at red (638 nm), green (554 nm), and blue (470 nm) wavelengths, the S5011 concentrations were adjusted to 2.25 wt%, 2.68 wt%, and 3.2 wt%, respectively. The mixtures were magnetically stirred at 100 °C (the clearing point) for 2h to ensure homogeneity. Subsequently, the pre-prepared CLCs were doped with R6G and further dissolved in dichloromethane. The resulting mixture was sonicated to promote uniform dye dispersion, followed by stirring at 105 °C (above the clearing point) for 1 h. This process yielded a homogeneous R6G-CLC system in which both the CLC matrix and the R6G dye were fully dissolved.

Preparation of R6G-Doped Cholesteric Liquid Crystal Microcapsules (R6G-CLCMs)

R6G-CLCMs were synthesised via an interfacial polymerisation. First, the R6G-CLC was thoroughly blended with methyl methacrylate (MMA) and the radical initiator ABVN. The resulting organic phase was then added dropwise at 0.5 mL/min into 60 mL of a 6 wt% aqueous PVA solution, whilst maintaining a constant temperature of 60 °C and stirring at 1400 rpm using a magnetic stirrer equipped with an olive-shaped PTFE stirring bar (Hunan Beekman Biotechnology Co., Ltd., Changsha, China). This procedure generated a stable oil-in-water (O/W) emulsion, in which the organic droplets containing the liquid crystal core and monomer were uniformly dispersed in the aqueous continuous phase. After 50 minutes of continuous stirring, the emulsion temperature was raised to 80 °C and held for a further 5 h to complete the free-radical polymerisation of MMA, yielding a robust PMMA shell encapsulating each microcapsule. The resulting suspension was allowed to stand, centrifuged, and washed twice with deionised water. A final concentrated dispersion of R6G-CLCMs was collected for subsequent use. For the preparation of dye-free cholesteric

liquid crystal microcapsules (CLCMs), the same procedure was applied, substituting the R6G-CLC with undoped CLC under identical conditions.

Preparation of Water-based R6G-CLCM Inks

The obtained R6G-CLCMs were dispersed in a 15 wt% PVA solution at a microcapsule-to-PVA weight ratio of 1:1.5 for mould casting and blade coating, or 1:1 for dispensing applications. To suppress coffee-ring effects and improve ink homogeneity, 0.01 wt% Silok 120 was added, and the mixture was homogenised using a vortex mixer, yielding a stable and well-dispersed water-based ink.

Characterisations

The microscopic textures and optical alignment of the samples were examined using a polarized optical microscopy (POM; DM2500, Leica Microsystems, Wetzlar, Germany). UV-vis diffuse reflectance spectra were recorded with a UV-vis-NIR spectrophotometer (UH4150, Hitachi High-Technologies, Tokyo, Japan) equipped with an integrating sphere. Fluorescence emission spectra were measured using a fluorescence spectrophotometer (F-4700, Hitachi High-Technologies, Tokyo, Japan). The prepared dispersions and inks were homogenised using a vortex mixer (MX-S, DRAGONLAB Scientific Co., Ltd., Beijing, China). Film thicknesses were determined with a digital micrometer (3V, HEMUELE Instruments, Zhejiang, China). The surface morphology and microstructure of the microcapsules and films were characterised by scanning electron microscopy (SEM; GeminiSEM 300, ZEISS, Oberkochen, Germany). Elemental composition was analyzed by energy-dispersive X-ray spectroscopy (EDS; XPLORE30, Oxford Instruments, Oxford, UK). The shell thickness of the microcapsules was measured using cryogenic scanning electron microscopy (Cryo-SEM; Regulus 8220, Hitachi High-Tech, Japan). Circularly polarised luminescence (CPL) spectra and luminescence dissymmetry factors (g_{lum}) were measured with a CPL spectrometer (CPL-300, JASCO Corporation, Tokyo, Japan). Fourier transform infrared (FTIR) spectra were collected using an FTIR spectrometer (Nicolet- iS20, Thermo Fisher Scientific, Waltham, MA, USA). Differential scanning calorimetry (DSC) were conducted on a DSC instrument (DSC25, TA Instruments, New Castle, DE, USA), and thermogravimetric analysis (TGA) were performed using a thermogravimetric analyser (TG 209 F3, Netzsch, Selb, Germany). Relative reflectance spectra were obtained with a fiber-optic spectrometer (AvaSpec-2048, Avantes, Apeldoorn, The Netherlands). A handheld spectrophotometer (Ci64, X-Rite Inc., Grand Rapids, MI, USA) was employed. Pattern engraving was performed using a laser engraving machine (3020, OSAI Laser, China). Photographs of samples and patterned films were captured with a digital camera (α7 IV, Sony Corporation, Tokyo, Japan) equipped with an FE 24-105 mm F4 G OSS lens.

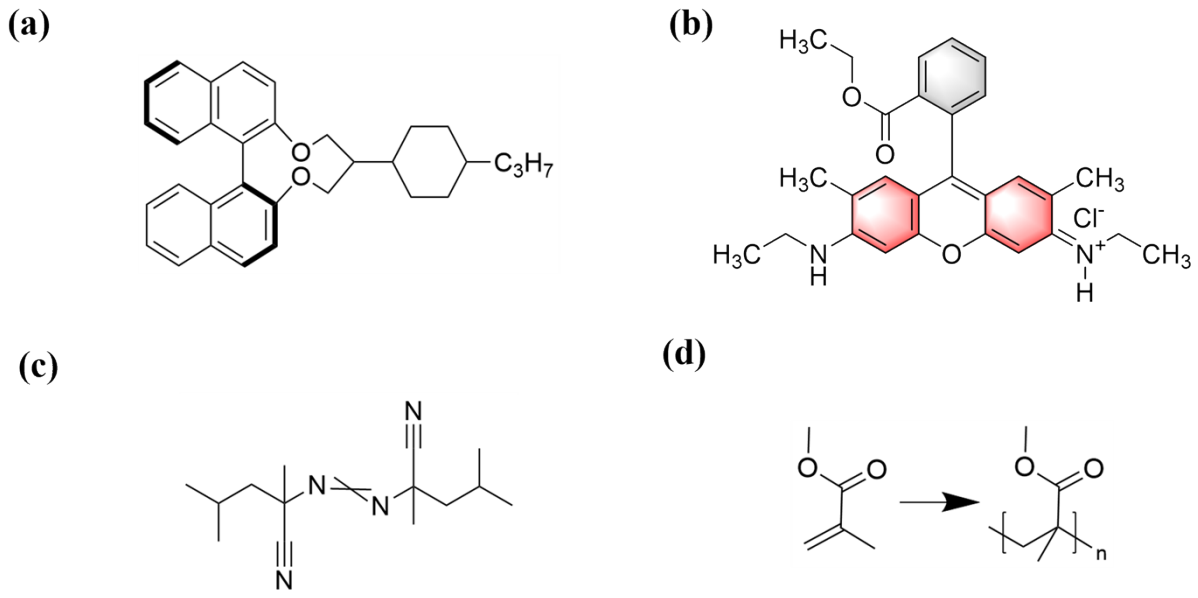

Figure S1. Chemical structures of the components used for the preparation of R6G-CLCMs: (a) S5011 (left-handed chiral dopant based on an axially chiral BINOL moiety, highlighted in the structure), (b) Rhodamine 6G (R6G, fluorescent dye), (c) azobis (isoheptanenitrile) (ABVN, radical initiator), and (d) poly(methyl methacrylate) (PMMA) formed by initiated polymerisation.

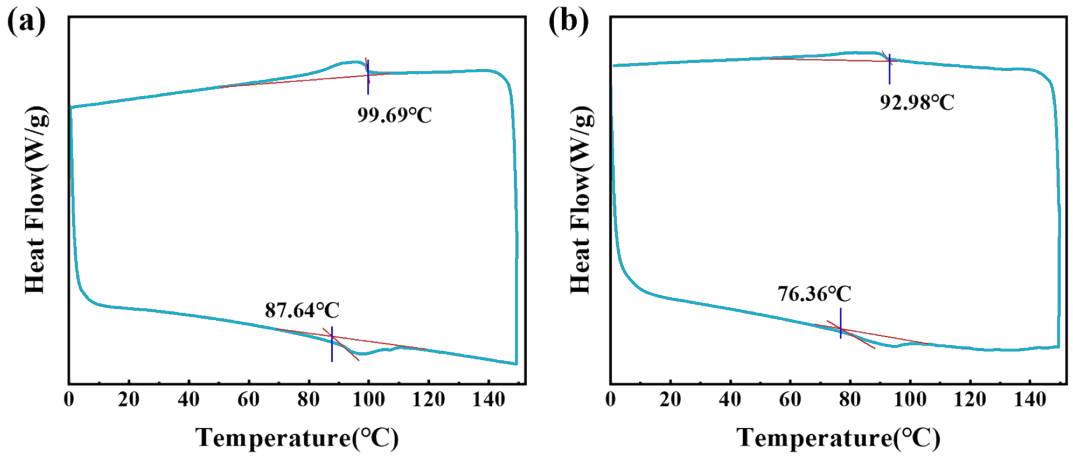

Figure S2. Differential scanning calorimetry (DSC) curves of CLC (a) and R6G-CLCMs (b).

The clearing point of the pure CLC sample was observed at 99.69 °C (a), whereas that of the R6G-CLCMs sample decreased to 92.38 °C (b). This reduction in transition temperature is attributed to the anchoring effect of the PMMA shell on the liquid crystal alignment and the disruption of the cholesteric helical structure by the incorporated R6G molecules.

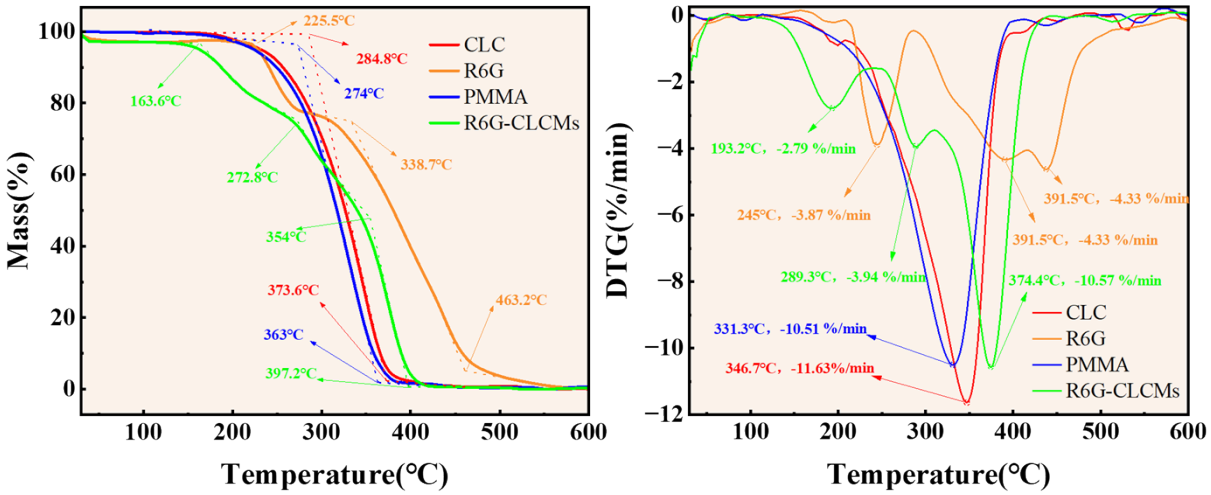

133

134 **Figure S3.** (a) TG and (b) DTG curves of CLC, R6G, PMMA, and R6G-CLCMs.

135 The TG/DTG profiles of CLC, R6G, PMMA, and R6G-CLCMs exhibit a clear progressive
136 decomposition behaviour that reflects the intrinsic thermal characteristics of each component
137 and confirms successful microcapsule construction. The CLC shows a rapid, single-step
138 volatilization with negligible residue, typical of low-molecular-weight liquid crystal materials.
139 R6G undergoes multi-stage decomposition with substantial carbonaceous residue, consistent
140 with its highly conjugated aromatic structure. PMMA displays a single dominant degradation
141 event associated with chain-scission depolymerisation, leaving nearly no residue, as expected
142 for a pyrolytic polymer. In contrast, R6G-CLCMs present a broadened, multi-stage composite
143 decomposition profile: low-temperature weight loss originates from the liquid crystal core and
144 trace surface-bound dye, whilst higher-temperature mass loss corresponds to overlapping
145 degradation of the LC/R6G core and the PMMA shell. The increased final residue reflects the
146 contribution of thermally stable R6G. Collectively, the combined thermal signatures
147 demonstrate that the microcapsules integrate the decomposition characteristics of all
148 constituents and exhibit synergistic multi-component behaviour, confirming the successful
149 formation of the core-shell R6G-CLCM structure.

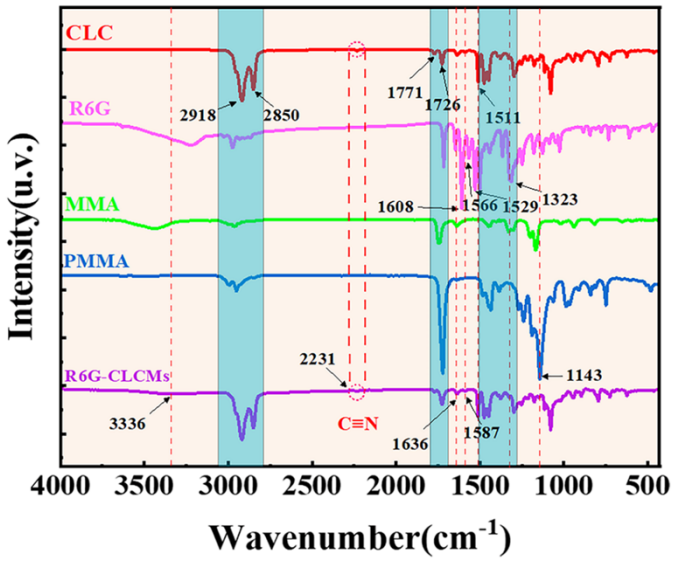

Figure S4. Fourier transform infrared (FTIR) spectra of R6G-CLCMs and their precursor components, including CLC, Rhodamine 6G, methyl methacrylate (MMA), and poly (methyl methacrylate) (PMMA).

The FTIR spectrum of the final R6G-CLCMs contains representative absorption features from all major components. The cholesteric liquid crystal exhibits its characteristic aliphatic stretching bands at 2918 cm^{-1} and 2850 cm^{-1}, together with the distinct –C≡N stretching vibration at 2231 cm^{-1}, confirming that both the alkyl backbone and terminal cyano groups remain intact after encapsulation. R6G preserves its molecular structure within the microcapsules, as evidenced by the broad –OH stretching band at 3336 cm^{-1} from its carboxylic acid group, the aromatic C=C stretching features in the 1500–1600 cm^{-1} region, and the coupled C–N / C–O vibration near 1323 cm^{-1}.The MMA monomer shows a well-defined C=C stretching band at 1636 cm^{-1}, which disappears in both PMMA and the R6G-CLCMs, confirming complete polymerisation. A prominent C=O stretching band at 1726 cm^{-1} in the R6G-CLCMs spectrum arises from overlapping contributions of the CLC matrix, the PMMA shell, and R6G, reflecting their coexistence within a physically encapsulated rather than chemically crosslinked structure. Collectively, these characteristic absorption features verify that the functional groups of CLC and R6G are retained, MMA is successfully polymerised into PMMA, and the resulting R6G-CLCMs form a stable, physically assembled multi-component microcapsule architecture.

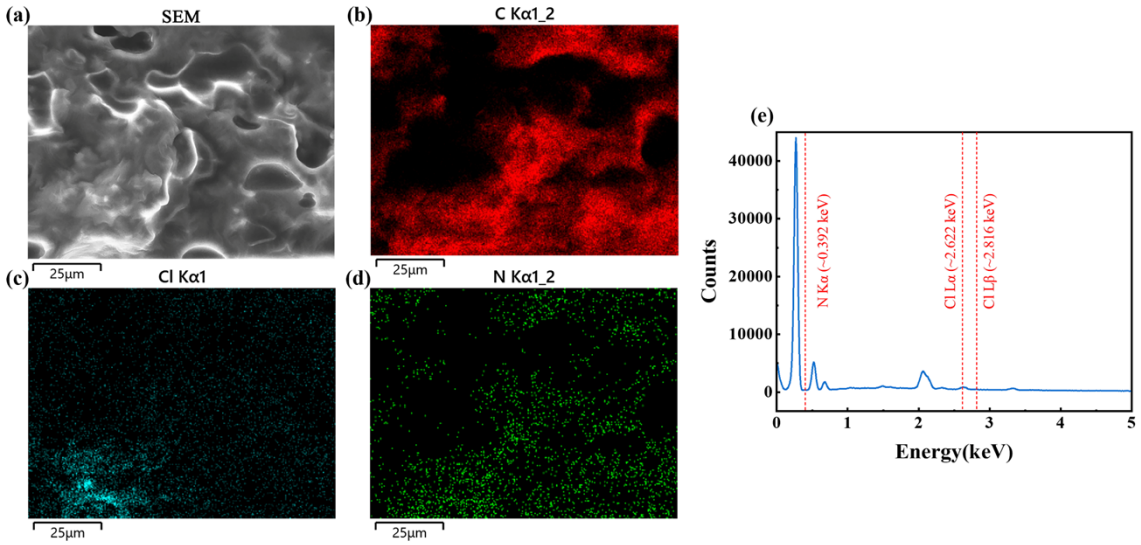

Figure S5. Energy-dispersive X-ray spectroscopy (EDS) analysis of the R6G-CLCMs/PVA composite film. (a) SEM image of R6G-CLCMs embedded in PVA matrix after electron beam bombardment Elemental mapping of (b) C, (c) Cl, and (d) N; (e) EDS spectrum with elemental peaks.

SEM image showing the R6G-CLCMs embedded in the PVA matrix after electron beam bombardment; local expansion and microcapsule rupture expose the internal regions, providing accessible windows for elemental analysis (a). Elemental mapping images of C, Cl, and N, respectively (b–d). The Cl element (c) shows a homogeneous distribution with localized enrichment, whilst the N element (d) appears discretely distributed, both indicating association with the R6G dye. (e) The EDS spectrum confirms the presence of key elements and their characteristic energy peaks: signals at 0.392 keV, 2.622 keV, and 2.816 keV correspond to N Kα, Cl Lα, and Cl Lβ, respectively, demonstrating the coexistence of N and Cl in the sample. Since the PVA matrix, PMMA shell, and CLC core contain neither nitrogen nor chlorine, these signals can be definitively attributed to the diethylamino group and the counter chloride ion of the R6G dye molecules. Combined observations from the SEM structural damage image, elemental distribution maps, and the EDS spectrum collectively confirm that R6G is successfully incorporated within the microcapsules and remains stably embedded in the PVA composite film.

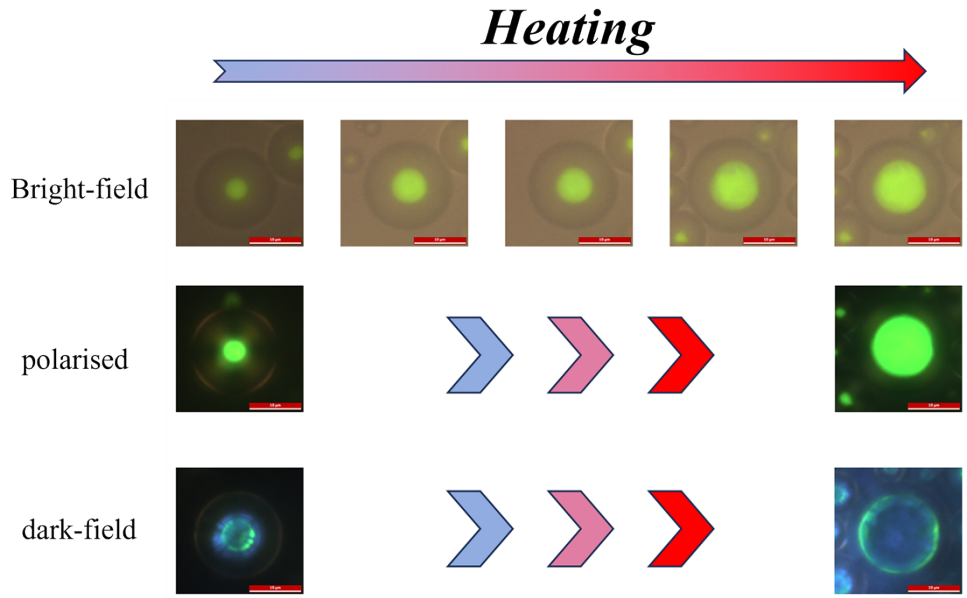

Figure S6. In optical microscopy images of a single R6G-CLCM under bright-field, polarised, and dark-field modes during mechanical compression. (Scale bar: 10 μm)

To further validate the structural stability and supporting capability of the microcapsules, an aqueous dispersion of R6G-CLCMs was drop-cast onto a glass slide and covered with a coverslip. The assembly was then placed on a heating stage maintained at 45 °C to control the slow evaporation of water, allowing real-time observation of structural changes in the same microcapsule during drying. In the bright-field mode, a central reflective bright spot within the microcapsule gradually intensified and expanded as the water evaporated. This phenomenon is attributed to the compressive force exerted by the coverslip during drying, which caused the initially spherical microcapsule to deform progressively into an ellipsoidal shape. This deformation led the liquid crystal core in the central region to transition from its initial radial alignment to an approximately planar alignment, resulting in enhanced light reflection and significantly increased brightness in this area. The polarised images provide further evidence for the evolution of the liquid crystal alignment. Initially, the R6G-CLCM displayed a characteristic Maltese cross pattern, indicating that the liquid crystal molecules were well aligned radially due to the anchoring effect of the polymer shell. As the drying progressed and the microcapsule became increasingly flattened under compression, the Maltese cross feature at the centre gradually weakened and eventually disappeared, whereas faint birefringent textures remained discernible around the periphery. This observation suggests that the shell

continued to maintain effective anchoring of the peripheral liquid crystal orientation even as the core region transitioned to a more planar structure.

Under dark-field illumination, the R6G-CLCM initially exhibited a distinct central green bright ring accompanied by six symmetrically distributed radial streaks of light, indicating that the internal liquid crystal molecules were in a well-ordered radial configuration, generating strong scattering and constructive interference effects. As water evaporation continued and the coverslip-induced compression increased, the microcapsule shape gradually evolved from a sphere to an ellipsoid, and the liquid crystal alignment underwent localized rearrangement. Consequently, the central bright ring became brighter and more diffuse, whilst the radial streaks progressively blurred, reflecting the gradual transition of the liquid crystal molecules from a radial to a more planar arrangement in the compressed state.

In summary, the in optical microscopy results clearly demonstrate that the R6G-CLCM microcapsules possess moderate flexibility under external compression. This mechanical deformation not only confirms the integrity and resilience of the capsule structure but also leads to a localized increase in the visual reflectance due to the reorganization of the liquid crystal core.

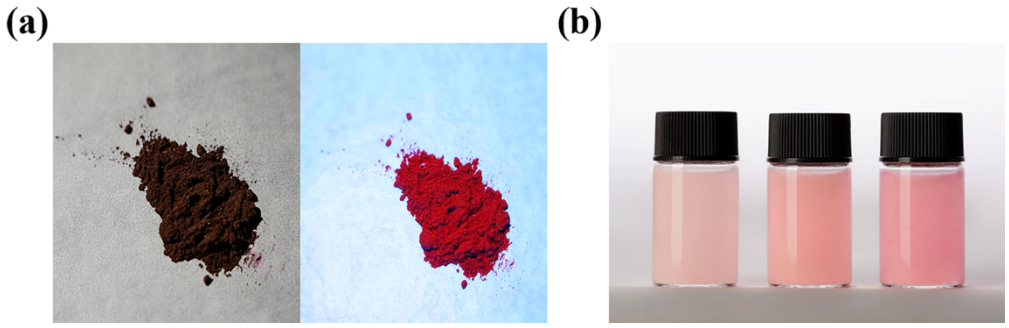

Figure S7. Photographs of R6G and R6G-CLCMs aqueous dispersions. (a) R6G under daylight (left) and under 360 nm UV light irradiation (right); (b) aqueous dispersions of R6G-CLCMs prepared with different R6G concentrations (0.05wt%, 0.1wt%, and 0.2wt%).

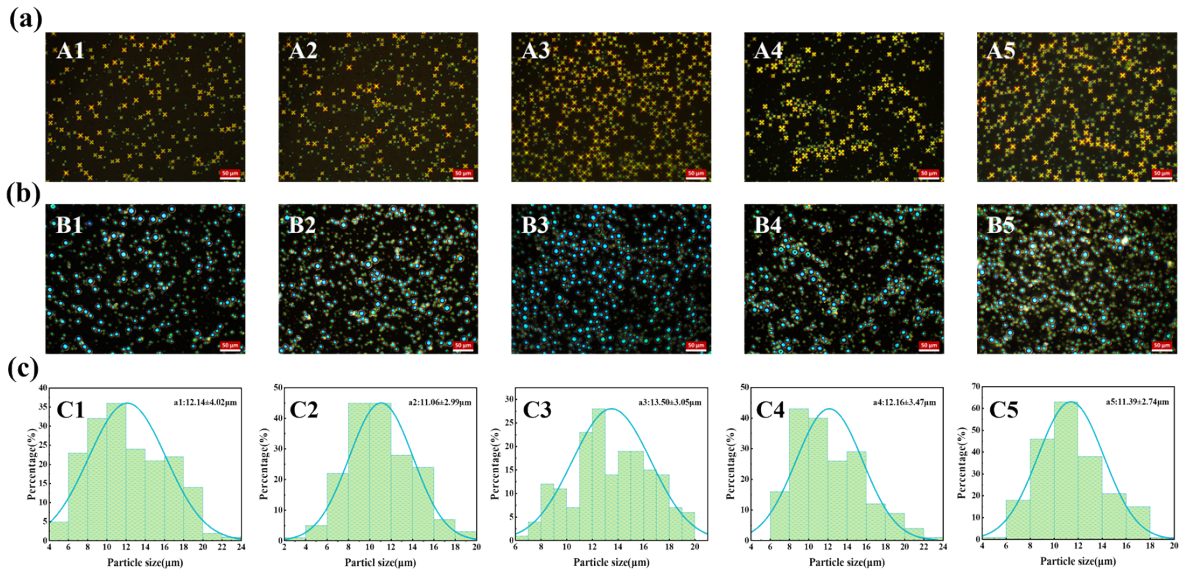

Figure S8. Polarised images (a), dark-field images (b), and particle size distribution (c) of R6G-CLCMs prepared with different R6G doping concentrations (0.05wt%, 0.1wt%, 0.15wt%, 0.2wt%, and 0.25wt%).(Scale bar: 50 μm)

In the polarised images (A1–A5), all R6G-CLCMs exhibit bright and well-defined Maltese cross patterns, indicating excellent radial alignment of the liquid crystal molecules within the microcapsules. The corresponding dark-field images (B1–B5) show each R6G-CLCM as a bright green dot further confirming the well-defined radial molecular orientation.

Panel (c) shows the particle size distribution calculated from over 180 sampling points per concentration. The results demonstrate that the average microcapsule diameter remains consistent at approximately 12 μm, irrespective of the R6G concentration. Minor deviations observed in the distribution are likely attributable to manual measurement variability and instrument error. Overall, the polarised and dark-field observations, combined with the size distribution analysis, confirm that the R6G-CLCMs maintain stable morphology and uniform radial alignment across varying dye concentrations.

Figure S9. Optical images of a mould-cast “orange” patterned R6G-CLCMs film under Daylight (left) and UV illumination (right), illustrating the impact of the coffee-ring effect.

During natural drying, the solvent evaporation causes radial outward flow, transporting microcapsules and dye molecules toward the edge of the mould. As a result, more R6G-CLCMs accumulate along the perimeter, forming a distinct coffee-ring pattern. This leads to a noticeable colour and fluorescence intensity gradient: the film edge appears darker and more fluorescent under UV light, whilst the central region is relatively uniform but less intense. The coffee-ring-induced non-uniform distribution adversely affects the homogeneity of structural colour, dye absorption, and fluorescence, underscoring the necessity for optimised ink formulations and drying control to suppress this effect in practical patterning applications.

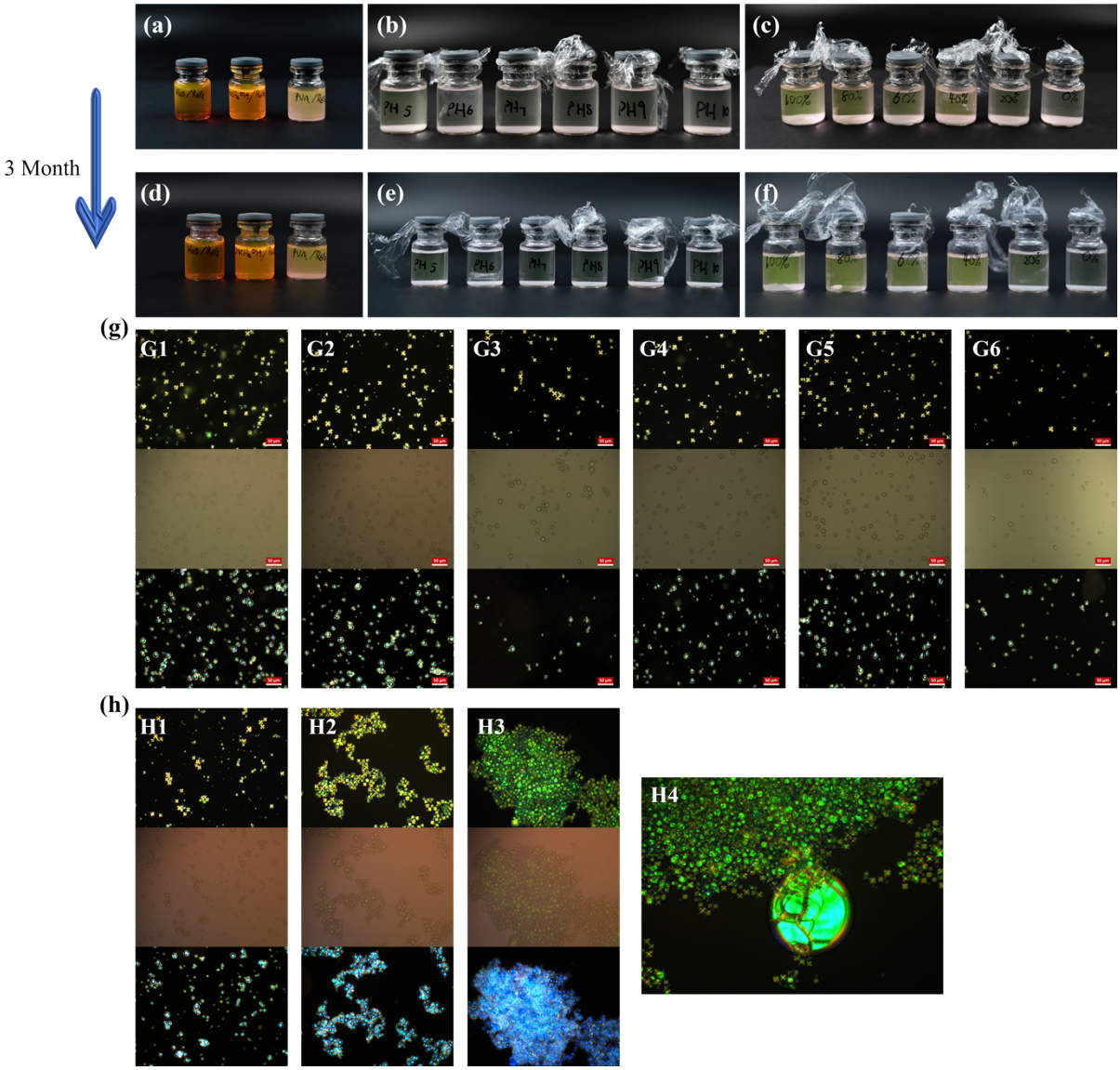

Figure S10. Environmental compatibility tests of R6G and R6G-CLCMs. (a) R6G dissolved in water, anhydrous ethanol, and 15 wt% PVA solution. (b) R6G-CLCMs stored in buffer solutions with different pH values (initial state). (c) R6G-CLCMs stored in ethanol solutions of varying concentrations (initial state). (d) Appearance of R6G-CLCMs after 3 months in different solvents. (e) Appearance after 3 months in different pH environments. (f) Appearance after 3 months in ethanol solutions of varying concentrations. (g) Optical microscopy of R6G-CLCMs under various pH conditions (G1–G6: polarised, bright-field, dark-field). (h) Optical microscopy under various ethanol concentrations.(Scale bar: 50 μm)

R6G was dissolved in water, anhydrous ethanol, and a PVA solution to observe its colour appearance. As shown in Figure S10a, the dye displayed distinct colours in these different solvents. The resulting R6G-CLCMs were stored in solutions with different pH values (5 to 10)

for stability testing. Initially, the sample at pH=3 exhibited a slightly yellow-green, while other pH conditions showed negligible colour change (Figure S10b). The microcapsules were also immersed in ethanol solutions with concentrations ranging from 0vol% to 100vol% (Figure S10c. Upon contact with ethanol, a yellow-green colour emerged and intensified with increasing ethanol concentration, likely due to dissolution of free R6G from the capsule surface. After three months of storage, no visible dye precipitation was observed in any solvent, indicating good compatibility of R6G with the microcapsule system (Figure S10d). Under neutral pH conditions, the R6G-CLCMs remained visually unchanged, while acidic or alkaline environments induced a slight yellow-green hue (Figure S10e). At ethanol concentrations exceeding 80vol%, aggregation and partial capsule damage were observed (Figure S10f). To further investigate the capsule integrity, samples from the different pH conditions were examined by optical microscope (Figure S10g). Images G1–G6 show the polarised, bright-field, and dark-field views, respectively. In polarised mode, R6G-CLCMs consistently displayed clear and uniform Maltese cross textures, indicating well-maintained radial alignment. In bright-field mode, each microcapsule appeared as a distinct, well-oriented green dot, and in dark-field mode, strong internal reflection was still evident. These results confirm that the optical properties of the microcapsules remained stable under various pH conditions.

Additionally, samples stored in varying concentrations of anhydrous ethanol were also analysed. At ethanol concentrations below 60vol% (H1–H3), the R6G-CLCMs maintained good optical performance under polarised, bright-field, and dark-field observations, although aggregation increased. As the ethanol concentration increased, significant damage and rupture occurred at 80vol% (H4), leading to leakage of the liquid crystal core. Furthermore, a few minutes later, even the samples at lower concentrations (H1–H3) exhibited similar rupture behaviour as H4. In contrast, the microcapsules stored in different pH conditions remained relatively stable. Therefore, it can be concluded that high-concentration anhydrous ethanol negatively affects the mechanical integrity of R6G-CLCMs, causing embrittlement of the PMMA shell.

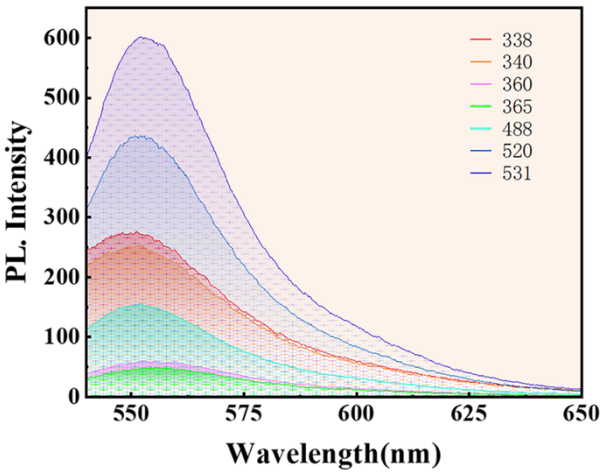

Figure S11. Different excitation wavelengths were employed to investigate the visible-region emission characteristics of the R6G-CLCMs.

Under excitation at 338 nm and 340 nm, the fluorescence intensity was relatively strong, with the highest emission peak observed at 531 nm and a secondary peak at 520 nm. Emission intensities at other excitation wavelengths were comparatively lower. In this study, 531 nm excitation was selected for analyzing the spectral properties of dye-doped liquid crystals and microcapsule-based films; 360 nm excitation was used for photographing real film samples; and 520 nm excitation was chosen for CPL measurements.

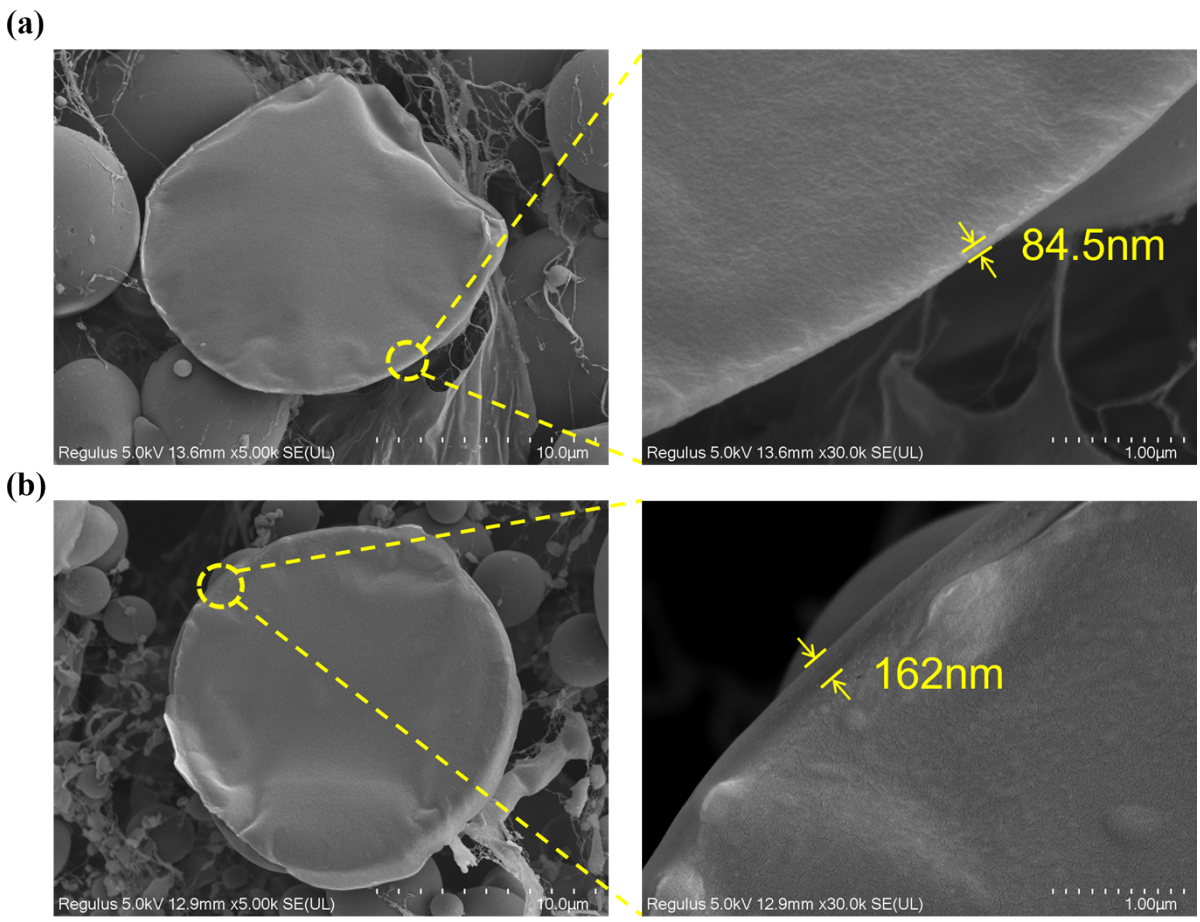

Figure S12. Cryo-SEM images of R6G-CLCMs synthesised with different MMA contents. (a) Microcapsules prepared with 0.8 g MMA; the enlarged image on the right corresponds to the circled region in (a), revealing a PMMA shell thickness of approximately 84.5 nm. (b) Microcapsules prepared with 1.2 g MMA; the enlarged image on the right corresponds to the circled region in (b), showing an increased shell thickness of approximately 162 nm.

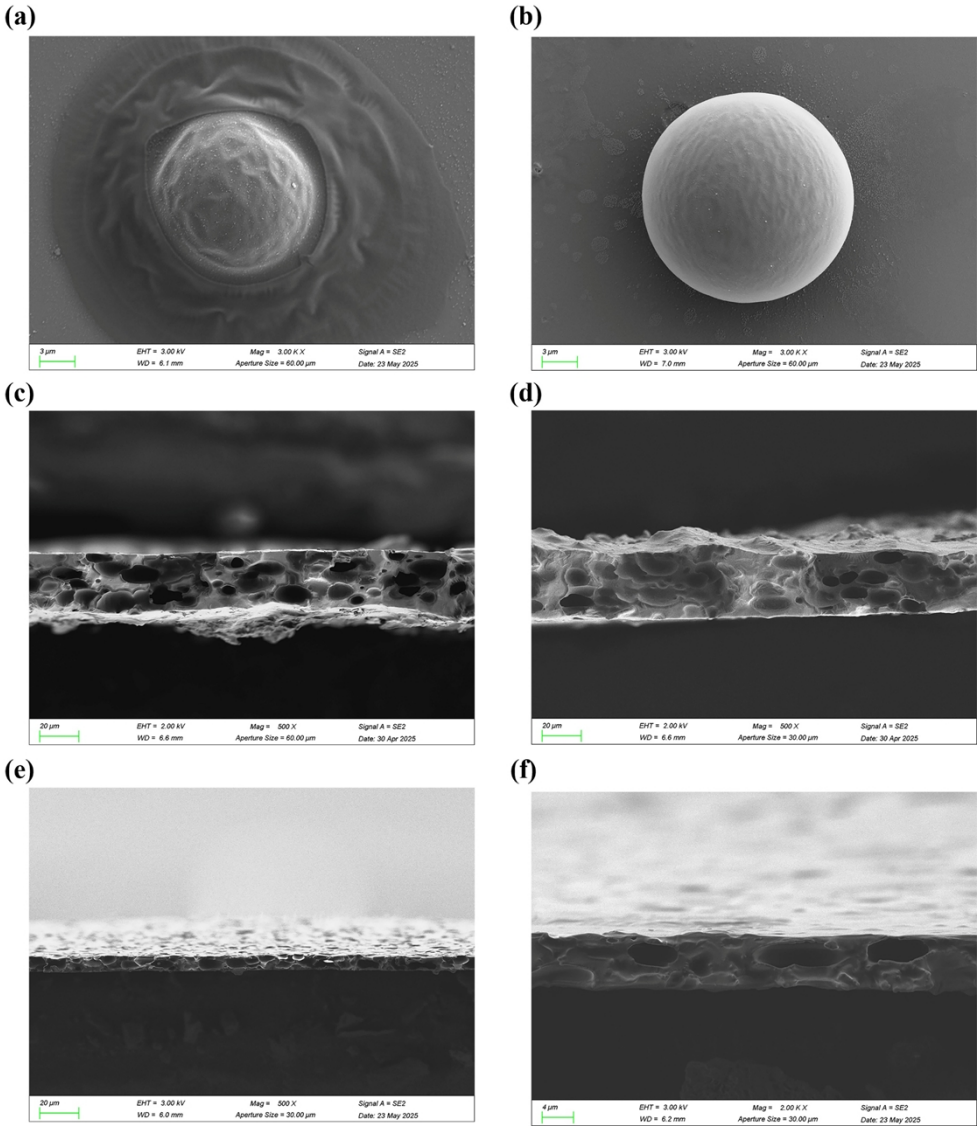

Figure S13. Morphology of individual R6G-CLCMs microcapsules and cross-sectional structures of films prepared under different fabrication conditions. (a) R6G-CLCMs synthesised with 0.8 g MMA (thin-shell); (b) R6G-CLCMs synthesised with 1.2 g MMA (thick-shell); (c) Cross-section of 55 µm mould-cast film (liquid nitrogen fractured); (d) Cross-section of 85 µm mould-cast film (liquid nitrogen fractured); (e) Cross-section of blade-coated film (liquid nitrogen fractured); (f) Cross-section of blade-coated film (mechanical blade cut).

SEM image of microcapsules synthesised with 0.8 g MMA as the shell monomer shows pronounced surface wrinkles and shape shrinkage, indicating insufficient structural stability (a). In contrast, microcapsules prepared with 1.2 g MMA exhibit a more uniform spherical shape with a smooth and intact surface (b). Due to the absence of a crosslinker and the use of free-radical polymerisation, the PMMA shells adopt a linear polymer structure without covalent crosslinking support, resulting in poor self-supporting capability at lower MMA

content. Cross-sectional SEM images of films prepared by mould casting with thicknesses of 55 μm (c) and 85 μm (d) after liquid nitrogen fracturing reveal densely packed microcapsules within the film matrix. Some capsules are slightly deformed due to compression but largely retain their spherical geometry, with no obvious rupture caused by the pressure from adjacent layers. The intact internal structure indicates good compressive resistance of the material. By comparison, films fabricated by blade coating exhibit higher surface smoothness and uniformity. Under liquid nitrogen fracturing conditions (e), partial capsule rupture can be observed, but the original spherical morphology is still recognizable, demonstrating adequate self-support. Under mechanical cutting using an ordinary blade (f), some microcapsules are broken, causing localized leakage, whilst others maintain their elliptical shape due to compressive deformation, further confirming the morphological integrity of the capsules within the film.

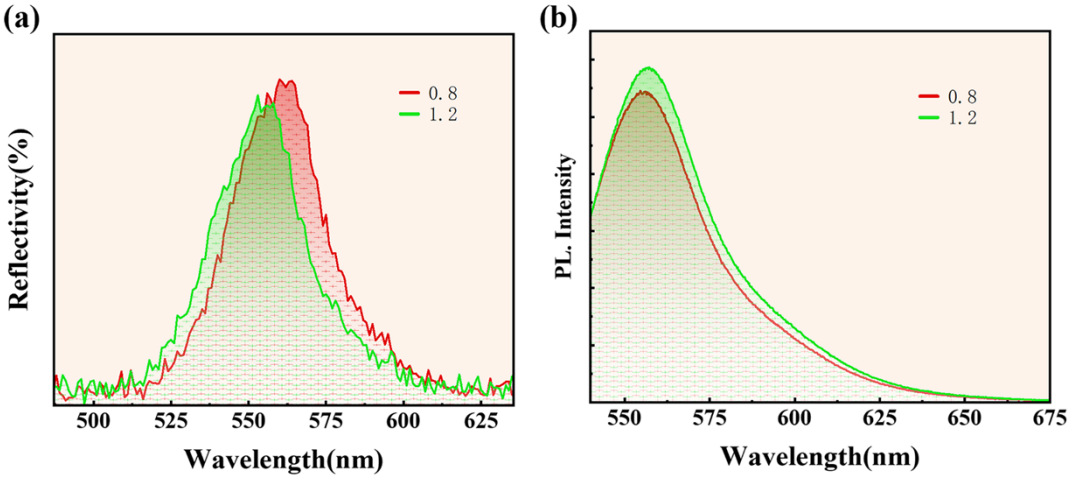

Figure S14. Reflectance and fluorescence properties of R6G-CLCMs with different shell thicknesses. The microcapsules were prepared with 0.8 g MMA (thin shell) and 1.2 g MMA (thick shell) under otherwise identical conditions. (a) Reflectance spectra. (b) Fluorescence emission spectr.

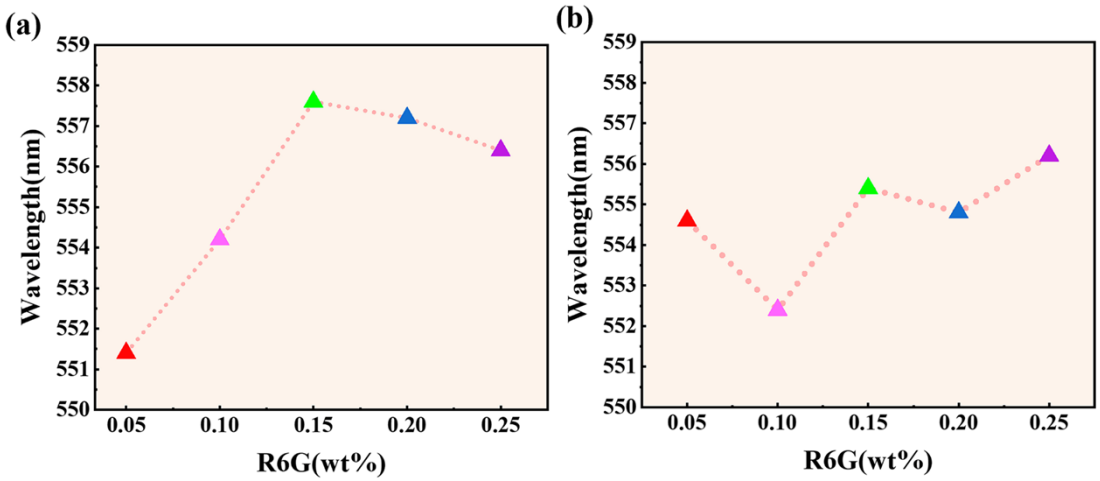

349

350 **Figure S15.** Fluorescence peak position trends of R6G-CLCMs at various dye concentrations.
351 (a) Thick-shell microcapsules (1.2 g MMA): Fluorescence emission peak trend. (b) Thin-shell
352 microcapsules (0.8 g MMA): Fluorescence emission peak trend.

353

354

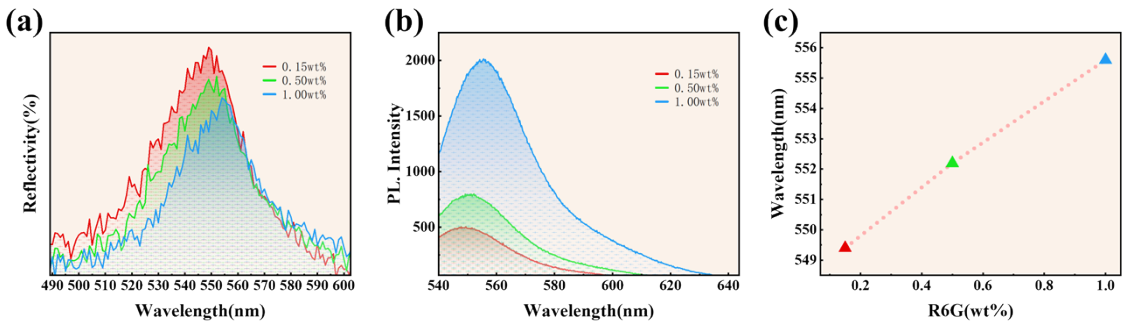

355

356 **Figure S16.** Optical properties of R6G-CLCMs films with higher R6G doping concentrations
357 prepared by blade coating. (a) Reflectance spectra (b) fluorescence emission spectra. (c)
358 Fluorescence emission peak wavelengths.

359

360

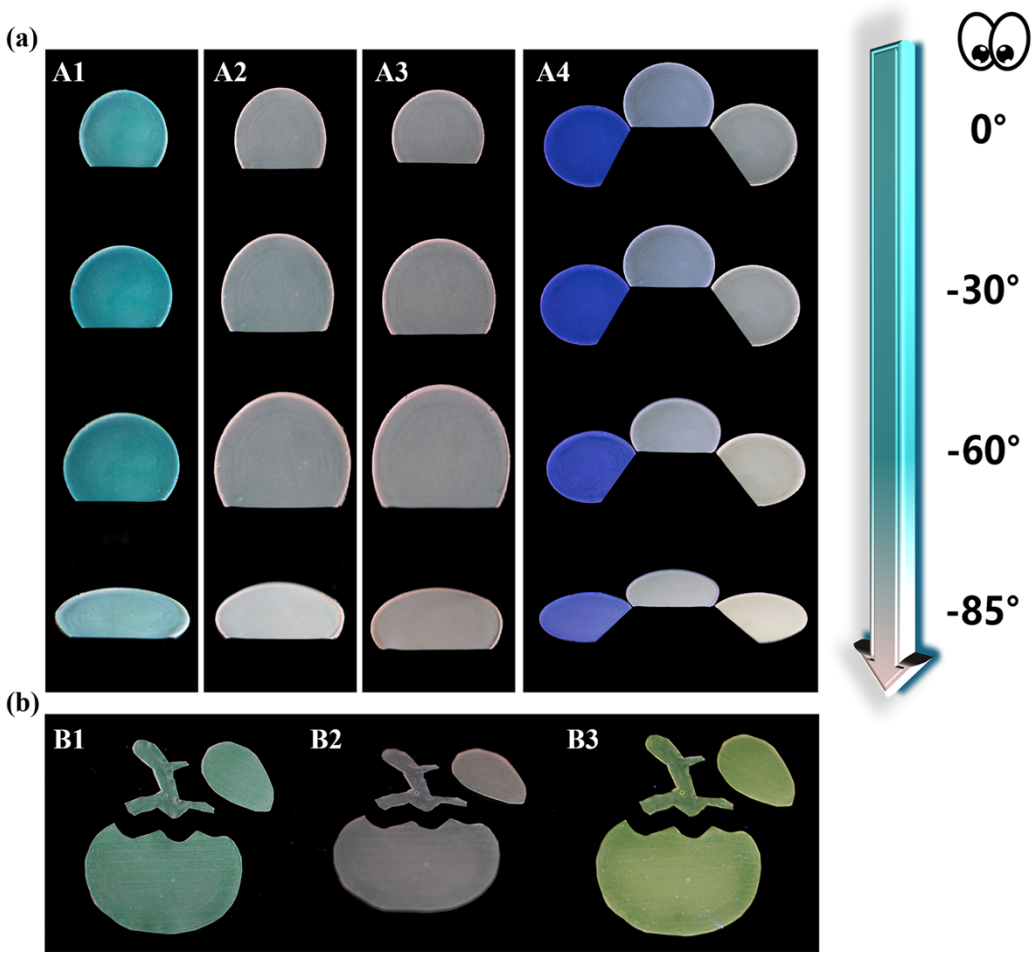

Figure S17. Mould-cast films fabricated with different concentrations of R6G-CLCMs. (a) Angle-dependent optical and fluorescence responses of films containing 0.05 wt% (A1), 0.15 wt% (A2), and 0.25 wt% (A3) R6G-CLCMs. A4 shows the combined fluorescence images of A1–A3 under UV light at different viewing angles. (b) Structural colour (B1), dye absorption (B2), and fluorescence emission (B3) of a film prepared using a higher PVA dilution ratio (1:2.5).

For samples A1–A3, R6G-CLCMs with concentrations of 0.05 wt% (A1), 0.15 wt% (A2), and 0.25 wt% (A3) were each mixed with a 15% PVA solution at a weight ratio of 1:1.5. The mixtures were slowly injected into custom moulds using a syringe and dried naturally at room temperature to form the films shown. The optical appearance of these films was observed over a viewing angle range from 0° to −85°. As the viewing angle decreased, the microcapsule films gradually appeared pinkish. This is because at 0°, the structural colour of the liquid crystals is relatively strong and dominates the appearance; however, as the angle decreases, the structural reflection is increasingly masked by the inherent colour of the R6G dye, leading

to a more pronounced display of the dye colour. Consequently, fluorescence is enhanced at these lower angles, which is corroborated by the fluorescence images under varied angles shown in A4.

Due to the use of 1.2 g MMA to prepare a thicker PMMA shell, the R6G-CLCMs themselves exhibit a slightly pinkish hue. To reduce this effect and better demonstrate the distinct optical features, another film was prepared by mixing R6G-CLCMs (0.15wt%) with a 15wt% PVA solution at a weight ratio of 1:2.5 and thoroughly homogenised. The resulting film (b) further highlights three key aspects: the clear cholesteric liquid crystal structural colour (B1), the intrinsic pinkish colour of the R6G-loaded material (B2), and the yellow-green fluorescence of the R6G-CLCMs under UV light (B3).

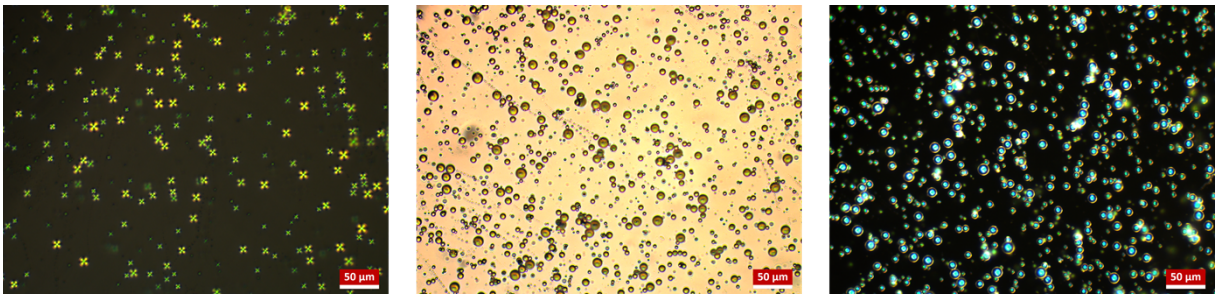

Figure S18. Polarized optical microscopy (POM) images of dye-free cholesteric liquid crystal microcapsules (CLCMs) observed under crossed-polarised, bright-field, and dark-field conditions. (Scale bar: 50 µm)

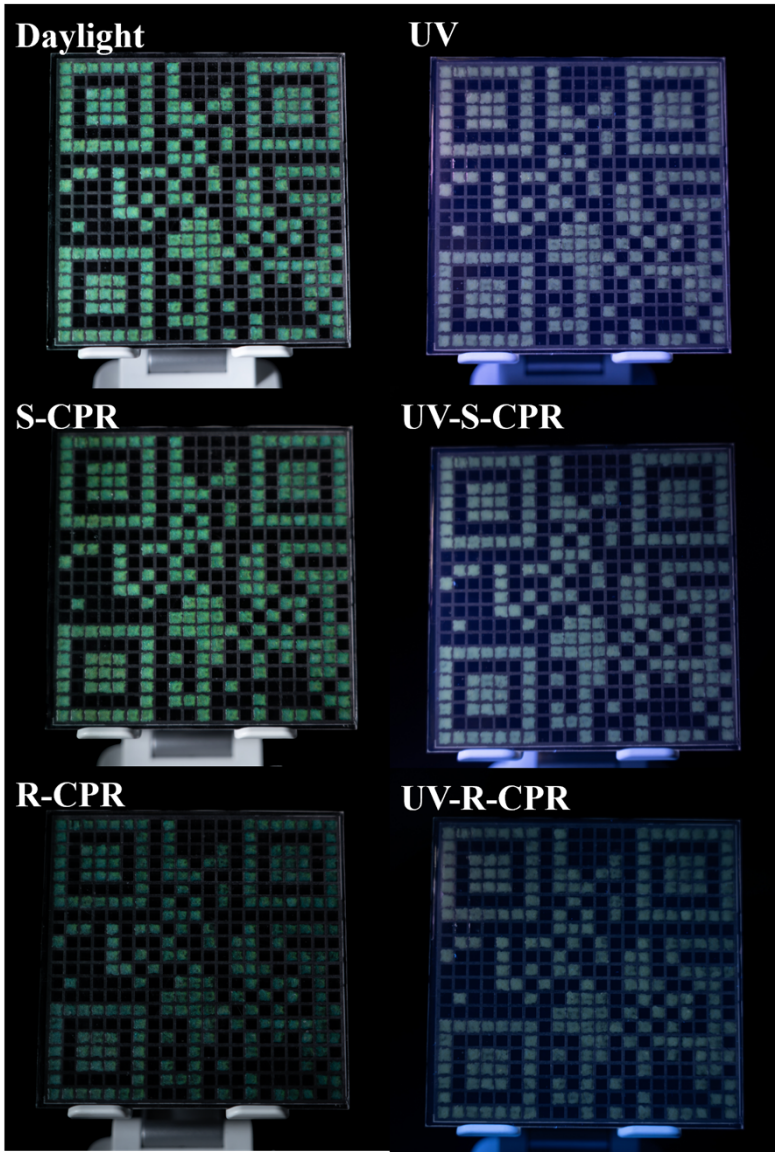

392

393 **Figure S19.** Polarised optical images of a single-ink R6G-CLCMs QR code on a black substrate
394 under daylight and UV illumination.

395

396

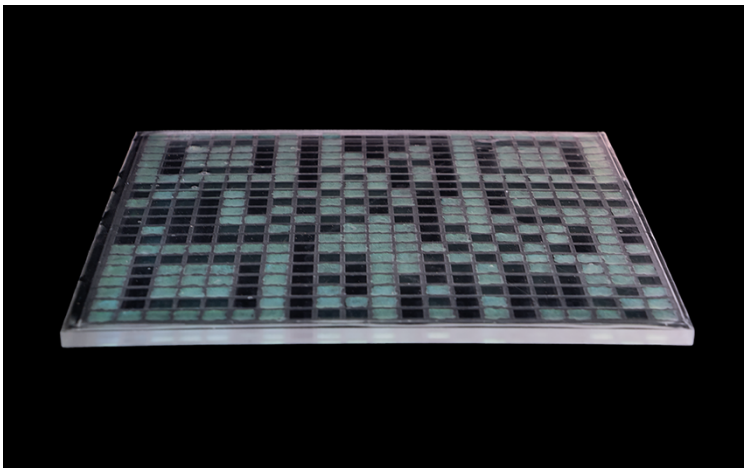

Figure S20. Angle-dependent optical images of a single-ink R6G-CLCMs QR code on a black substrate, showing a colour shift from green structural colouration to pink dye absorption with changing viewing angle.